EARTH SURFACE PROCESSES AND LANDFORMS
Earth Surf. Process. Landforms (2017)

Published online in Wiley Online Library
(wileyonlinelibrary.com) DOI: 10.1002/esp.4243

Transport of suspended sediments under the influence of bank macro-roughness

Carmelo Juez,* **Iria Bühlmann, Gaetan Maechler, Anton J. Schleiss and Mário J. Franca**
École Polytechnique Fédérale de Lausanne (EPFL), Laboratoire de Constructions Hydrauliques (LCH), Lausanne, Switzerland

Received 21 December 2016; Revised 22 August 2017; Accepted 31 August 2017

*Correspondence to: Carmelo Juez, École Polytechnique Fédérale de Lausanne (EPFL), Laboratoire de Constructions Hydrauliques (LCH), Lausanne, Switzerland.
E-mail: carmelo.juez@epfl.ch

ESPL
Earth Surface Processes and Landforms

ABSTRACT: River restoration works often include measures to promote morphological diversity and enhance habitat suitability. One of these measures is the creation of macro-roughness elements, such as lateral cavities and embayments, in the banks of channelized rivers. However, in flows that are heavily charged with fine sediments in suspension, such as glacier-fed streams and very low-gradient reaches of large catchment rivers, these lateral cavities may trap these sediments. Consequently, the morphological changes may be affected, and the functionality of the restoration interventions may be compromised. Herein, we analyse the influence of these macro-roughness elements on the transport of fine sediments in the main channel. Laboratory tests with uniform flow charged with sediments in a channel with banks equipped with large-scale rectangular roughness elements were carried out. The laboratory experiments covered a wide range of rectangular cavity geometrical configurations and shallowness ratios. The influence of key parameters such as flow shallowness, geometric ratios of the cavities and initial sediment concentration was tested. Surface particle image velocimetry, sediment samples and temporal turbidity records were collected during the experiments. The amount of sediments captured by the cavities, the temporal evolution of the concentration of sediments in suspension and the flow hydrodynamics are cross-analysed and discussed. It is shown that the trapping efficiency of the macro-roughness elements is a clear function of the channel geometry and the shallowness of the flow. Copyright © 2017 John Wiley & Sons, Ltd.

KEYWORDS: bank macro-roughness; river embayments; lateral cavities; fine sediments; sediment transport in suspension; hydrodynamics

Introduction

The natural course and geometry of rivers have been artificially channelized by human activities for different purposes (land expansion, flood protection, agriculture). This human intervention has in turn caused an alteration in the continuity of the sediment transport and an impoverishment of the morphology of rivers (Allan and Castillo, 2007; Klosch and Habersack, 2017). Often, due to human constructions such as dams or other in-stream infrastructures, the natural equilibrium between the incoming and outgoing fluxes of sediments has been broken (McCartney, 2009), leading to the following: (i) sediment-deficit situations, where the flow capacity of transport is higher than the influx of sediments; or (ii) sediment-excess situations, where the flow capacity of transport is lower than the influx of sediments. A twofold local morphological response to these alterations of the natural sediment balance may occur: on the one hand, bed erosion and instability of riverbanks in areas where there is a sediment deficit; and, on the other hand, deposition and riverbed clogging in areas with sediment excess (Kondolf, 1997).

From an ecological point of view, disruption of the sediment cycle has important consequences for riverine habitats: fine suspended sediments, in particular, transport vectors of nutrients that contribute to algal growth (Von Bertrab *et al.*, 2013) and to the creation of areas with differentiated velocity values with potential for the the fixation of fish and vegetation (Wood and Armitage, 1997; Kemp *et al.*, 2011). If in excess, however, fine sediments may clog the hyporheic region, disrupting the vital space for benthic communities and impeding the vertical connectivity between ground and surface waters through the riverbed (Sternecker *et al.*, 2013; Baxter and Hauer, 2000).

Channelized rivers often display a straight path and monotonous river banks. This is in contrast to natural rivers, where high morphological diversity can be found from the grain scale (boulders and clusters) to the reach (banks, pools, riffles) and valley (braided and meandering channels) scales. A measure to promote morphological diversity and enhance habitat suitability is to add macro-roughness elements (also called cavities and lateral embayments) ti the lateral river banks. In Japan, the so-called Wandos (i.e., areas lateral to the main flow where the hydraulic characteristics are different) have ecological importance, serving as fish spawning and nursery habitats (Nezu and Onitsuka, 2002; Uno *et al.*, 2013). Ribi *et al.* (2014) studied the ability of lateral cavities in river channels to be used as a refuge for juvenile fish in rivers affected by hydropeaking.

In rivers heavily charged with fine sediments in suspension, these lateral cavities or embayments may trap the fine sediments traveling within the water, which, if excessive, may jeopardize their functionality. For example, this may occur in glacier-fed streams such as those in the upper Rhone

River in Switzerland, which are charged with fine sediments resulting from the erosion of the underlying glacier's bottom; in very low-gradient reaches of large catchment rivers; and after dam operations, causing flushing of the fine sediments accumulated in the reservoir.

Cavities or local widenings obtained by groynes may also be used to capture sediments laterally, maintaining a central navigable channel, as in the historical case of the *Girardon casiers* in the lower Rhone (France). These sediment traps may combine channel widening with the lowering of the channel bed (Hudson, 2002).

Finally, harbours in rivers may be conceptualized as cavities lateral to the main river flow. Depending on their geometry and flow characteristics, these cavities may be subjected to siltation of material transported in the main stream (Langendoen *et al.*, 1994; Van Schijndel and Kranenburg, 1998).

The impact of lateral embayments on the hydrodynamics, and to some extent on the sediment transport in open-channel flows, has been already thoroughly analysed. The *seiche* occurring in the so-called dead zones of the flow, corresponding to oscillations of the water surface, have long been known to condition the hydrodynamics of such lateral cavities (Kimura and Hosoda, 1997; Rivière *et al.*, 2010; Meile *et al.*, 2011b; Akutina, 2015). The mass and momentum exchange mechanisms between the main flow and lateral cavities for turbulence processes occurring in groyne fields have been studied experimentally (Uijttewaal *et al.*, 2001; Le Coz *et al.*, 2006; Weitbrecht *et al.*, 2007; Rivière *et al.*, 2010; Uijttewaal, 2014; Akutina, 2015; Mignot *et al.*, 2017) and numerically (Hinterberger *et al.*, 2007; McCoy *et al.*, 2008). Meile *et al.* (2011a) and Sukhodolov (2014) analysed the effect of macro-roughness elements positioned in the channel bank in the flow resistance. The role of sediment siltation in groyne fields for the sediment budget of rivers was investigated by Abad *et al.* (2008); Ten Brinke *et al.* (2004); Yossef and de Vriend (2010); Henning and Hentschel (2013). Recently, Sanjou and Nezu (2013) analysed, for a constant planar configuration of rectangular embayments, the effect of bed slope on the mass and the momentum exchange between inner and outer flows.

Nevertheless, laboratory experiments relating the hydrodynamics and morphodynamics of lateral embayments are scarce and difficult to carry out (Henning and Hentschel, 2013), since sedimentation processes are related to the variability of discharge (or flow aspect ratio), geometrical configuration of the river banks and the sediment concentration transported in the flow. Thus far, only a few details about measured sedimentation in laboratory channels under such conditions can be found (Sukhodolov *et al.*, 2002). In examples given in the literature, it is common to derive sedimentation patterns from the flow patterns observed in experimental channels and in the field. The morphological evolution of deposition in the lateral cavities is governed by these flow patterns. Nevertheless, it is still unknown to what extent the location and magnitude of the flow patterns (eddies) inside the cavities influence the amount of fine material trapped in embayments.

To address the morphological response of these lateral embayments to flows heavily charged with fine sediments in suspension, systematic laboratory tests in an open channel were carried out with a large number of different geometries of wall macro-roughness elements created by rectangular cavities. These cavities may be seen as idealized artificial macro-roughness elements that perturb the flow (Morris, 1955; Lawrence, 1997). In Lawrence (1997), differences were noted in hydraulic regimes under well-inundated, marginally inundated and partially inundated flow situations, depending on the size of the elements and the water depth. The focus of that study was the impact of these macro-roughness elements in overland flows during flooding events. In the present work, however, the lateral embayments are never flooded; i.e., the top surface of the walls which forms the cavities are always without water. Three different discharges, representative of low, medium and large shallowness situations, were tested under uniform flow conditions. The maximum capacity of the transport of sediments in suspension was imposed for each case at the beginning of the tests.

Three practical goals motivate this research: (i) to evaluate the impact of lateral embayments in hydraulics as a function of flow conditions and cavity geometry; (ii) to determine the amount and speed of fine sediment trapping related to the geometry of the lateral embayments; and (iii) to answer to what degree the cavities are filled with fine sediment. For interventions aiming at habitat enhancement, this last question is crucial: partial filling of the cavities promotes the appearance of areas with high and low velocities with the potential to create hydromorphodynamic diversity, which is desirable.

The remainder of this paper is structured as follows: first, a detailed description of the experimental setup as well as the methods to analyse the morphological response to lateral embayments is provided. Then, the results are shown and discussed. Finally, conclusions drawn from the experimental research are provided.

Experimental Setup

Flume description

Experiments were performed in a closed-circuit hydraulic system (Figure 1) with the following components: (i) a 2 m long, 1 m wide and 1 m high upstream head tank; (ii) the experimental reach, a 7.5 m long, 1.0 m wide and 0.5 m high rectangular open channel with a longitudinal slope of 0.1% (typical slope for the subcritical flows in the Alpine valleys); and (iii) a 3.5 m long, 1 m wide and 1 m high downstream tank, in which a pump is installed, that collects the circulating flow. The fine sediments are mixed in the downstream tank, where the water is pumped to the upstream tank by a pipe system equipped with a valve to control the discharge, and a flow meter. Both upstream and downstream tanks are equipped with a system to enhance sediment mixing. The channel bottom is smooth and made of painted wood. Upstream, the transition between the head tank and the channel reach is made by a honeycomb-type flow tranquillizer. Downstream from the channel, a Venetian gate allows the flow depth to be controlled.

Macro-roughness configurations

The walls of the experimental reach were formed with concrete bricks (0.25 m long, 0.10 m wide and 0.19 m high), which were moved to form the lateral rectangular cavities. A prismatic channel width formed with these elements (configurations 1.0, 2.0 and 3.0 in Figure 2) was set as the reference for all tests. The several geometries of the rectangular embayments were inspired by the research performed by Meile *et al.* (2011a), who studied macro-rough flows. These geometries fall within the classification of large-scale roughness at both channel banks, following Morris (1955). The cavities are characterized by their length l, the distance between two cavities L and the lateral depth W (see details in Figure 2). These geometrical parameters were systematically varied, as shown in Figure 2.

The configurations may be defined by several geometrical ratios: cavity aspect ratio, AR $= W/l$, roughness aspect ratio,

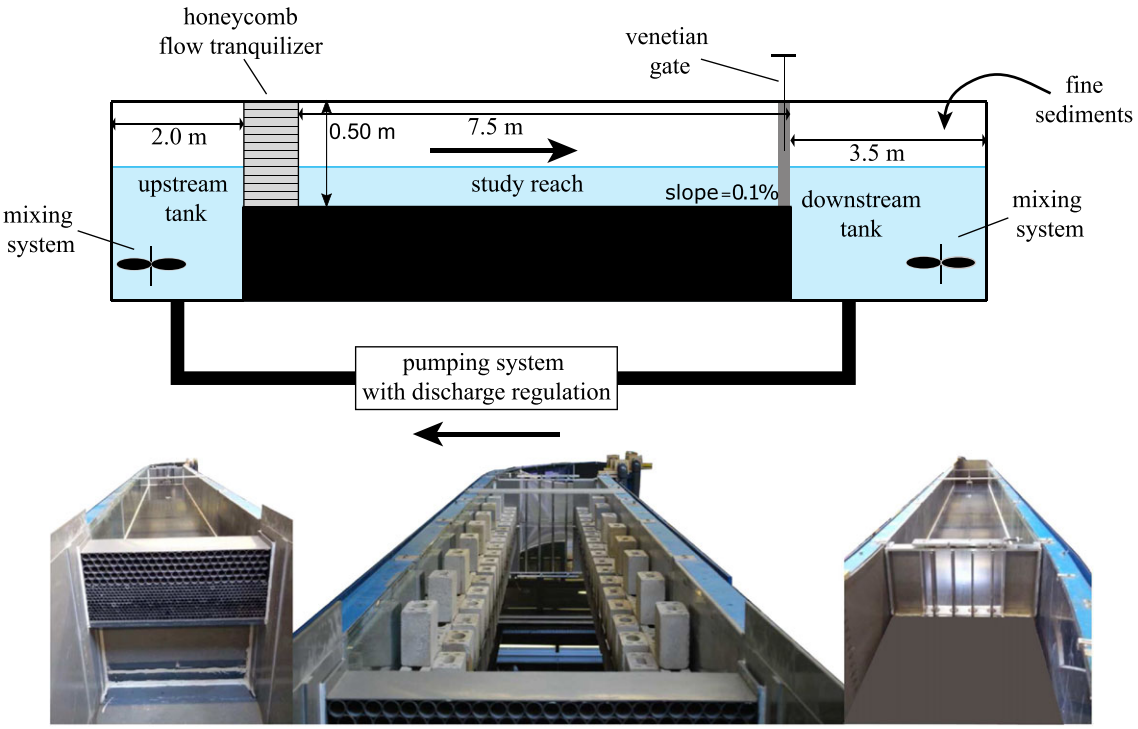

Figure 1. Sketch of the experimental flume (top); upstream view of the experimental channel (bottom left); rectangular channel with the macro-roughness elements (bottom centre); downstream view of the experimental channel (bottom right). [Colour figure can be viewed at wileyonlinelibrary.com]

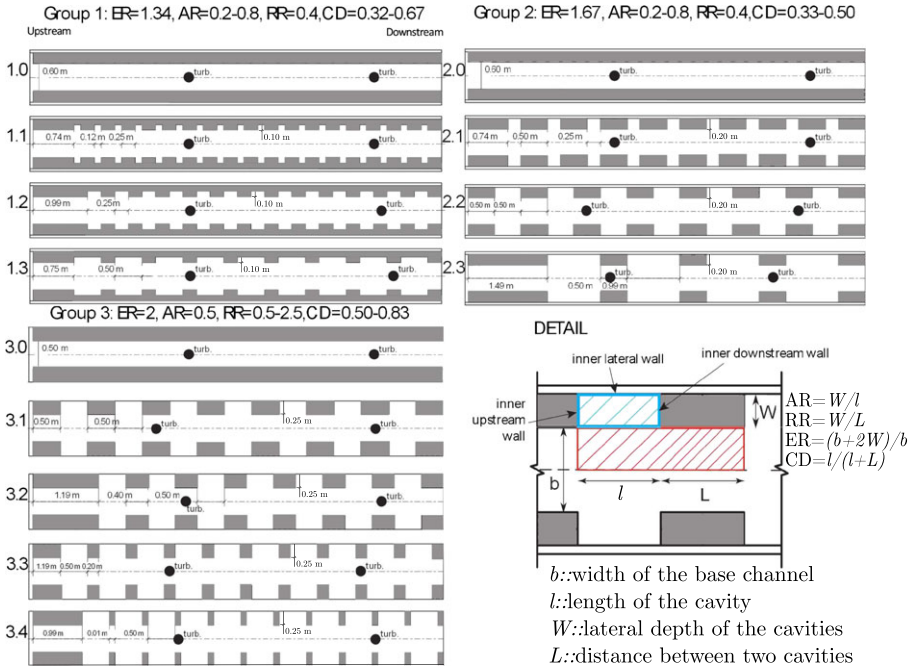

Figure 2. Geometric configurations tested and details of the definition of the geometric lengths of the macro-roughness configurations. The cavity area or inner region of the flow is represented in blue, and the outer region of the flow is represented in red. Given the symmetrical and periodical characteristics of the physical system, both the inner and outer regions define the basic flow element for analysis. The position of the turbidimeters is indicated for each configuration. [Colour figure can be viewed at wileyonlinelibrary.com]

RR = W/L, and expansion ratio, ER = $(b + 2W)/b$. The combination of these three different geometrical ratios with three different discharges led to 30 different symmetric geometrical configurations (see Table I. Another geometric parameter in Table I is the cavity density, CD = $l/(l + L)$.

Initial conditions

Three different discharges (representative of different degrees of shallowness) with their corresponding maximum capacity sediment concentration were considered (Table II). The capacity sediment concentration was determined experimentally and corresponds to the maximum concentration that the flow is able to transport in suspension without the verification of deposition and transport by bedload. The three discharges correspond to different values of the ratio between the water height, h, and the channel width, b: b/h = 17.26–7.20. The shallowness influence is as a key parameter in these flows: shallow flows lead to quasi-2D turbulence structures, which are the net contributors to the mass exchange between the main flow and the lateral embayments (Uijttewaal *et al.*, 2001;

Table I. Summary of the ranges of the geometrical parameters tested in the laboratory (cf. Figure 2).

Group	Configuration	Expansion ratio (–) ER = $(b + 2W)/b$	Cavity aspect ratio (–) AR = W/l	Roughness aspect ratio (–) RR = W/L	Cavity density (–) CD = $l/(l + L)$
1	1.1	1.34	0.80	0.40	0.32
	1.2	1.34	0.40	0.40	0.50
	1.3	1.34	0.20	0.40	0.67
2	2.1	1.67	0.80	0.40	0.33
	2.2	1.67	0.40	0.40	0.50
	2.3	1.67	0.20	0.40	0.50
3	3.1	2.00	0.50	0.50	0.50
	3.2	2.00	0.50	0.60	0.56
	3.3	2.00	0.50	1.20	0.71
	3.4	2.00	0.50	2.50	0.83

Table II. Summary of the flow conditions for each flow rate tested and for each geometric group considered (cf. Figure 2).

Discharge	$Q_1 = 4.8\ \mathrm{l\,s^{-1}}$		$Q_2 = 8.5\ \mathrm{l\,s^{-1}}$		$Q_3 = 15.0\ \mathrm{l\,s^{-1}}$	
Geometric groups	1 & 2	3	1 & 2	3	1 & 2	3
Water depth, h (m)	0.035	0.035	0.050	0.050	0.070	0.070
Shallowness ratio, b/h (–)	17.26	14.40	12.08	10.08	8.63	7.20
Cross-section averaged velocity, u ($\mathrm{m\,s^{-1}}$)	0.227	0.272	0.295	0.353	0.355	0.425
Froude number, $Fr = u/\sqrt{gh}$ (–)	0.387	0.464	0.421	0.504	0.428	0.513
Reynolds number, $\mathrm{Re} = R_h u/\nu$ (–)	28487	33449	50568	58940	80645	93168
Initial concentration, c_0 ($\mathrm{g\,l^{-1}}$)	0.500	0.500	1.000	1.000	1.500	1.500
Settling velocity, v_s ($\mathrm{m\,s^{-1}}$)	0.00276	0.00276	0.00276	0.00276	0.00276	0.00276
Shear velocity, $v_* = \sqrt{gR_hS_o}$ ($\mathrm{m\,s^{-1}}$)	0.0175	0.0174	0.0205	0.0202	0.0236	0.0232
Particle Reynolds number, $\mathrm{Re}_p = v_s d_{50}/\nu$ (–)	0.552	0.552	0.552	0.552	0.552	0.552
Shear Reynolds number, $\mathrm{Re}_* = v_* d_{50}/\nu$ (–)	3.508	3.473	4.103	4.046	4.722	4.636
Rouse number, $R = v_s/\kappa v_*$ (–)	0.393	0.397	0.336	0.341	0.292	0.297
Suspension criterion, v_*/v_s (–)	6.36	6.29	7.44	7.33	8.56	8.40
Duration of the experiments (h)	3	3	4	4	5	5

Note: g refers to the gravity acceleration, R_h is the hydraulic radius, ν is the kinematic viscosity of the water, d_{50} is the mean diameter of the sediments, κ is the Von Karman constant and S_o is the bed slope.

Uijttewaal, 2014). The herein tested discharges correspond to shallow flows.

The Froude (Fr) and flow Reynolds numbers (Re), calculated for the flow in the reference channel are in the range of $0.387 < \mathrm{Fr} < 0.513$ and $28{,}487 < \mathrm{Re} < 93{,}168$; therefore, the experiments were conducted under subcritical and turbulent conditions. The flow depths and cross-section averaged flow velocities are between $0.035\ \mathrm{m} < h < 0.070\ \mathrm{m}$ and $0.227\ \mathrm{m\,s^{-1}} < U < 0.425\ \mathrm{m\,s^{-1}}$, respectively.

Polyurethane artificial sediments were considered in all the experiments. The properties of this material are: density 1,160 $\mathrm{kg\,m^{-3}}$, grain size $d_{50} = 0.2$ mm. The mean diameter of particles was chosen to be within the range of non-cohesive fine sediment, 0.062–0.5 mm, according to Van Rijn (2007), and following the grain size that can be found in the Rhone River (Federal Office for the Environment, 2016). The Rouse numbers were $0.297 < P < 0.397$. The artificial nature of these sediments was preferred to natural clay–silty material to avoid algal and biofilm growth.

Froude similarity is usually considered in free-surface flows when the gravity and inertial forces are dominant over other types of forces (such as viscous or buoyancy forces; Imran *et al.*, 2017). This type of similarity implies a constant relation between velocities in the model and in the experiments. This would lead to low settling velocities in the case of suspended sediment and, consequently, the use of very small sediments with the risk of cohesion among particles. Nevertheless, this problem is well known for suspended mobile-bed experiments, and a reduced sediment density was considered to ensure suspended load transport. Therefore, this has no impact on the Rouse number or on the suspended load transport regime of the experiments. It simply means that the settling velocity in the experiments is exaggerated to respect the Froude similarity (de Vries, 1993; Yossef and de Vriend, 2010).

Conversely, the initial concentration was chosen in order to meet roughly the maximum transport capacity of the flow to transport the sediments in suspension. This depends on the hydraulic conditions imposed in the channel, and values of the initial concentration were determined experimentally, resulting in 0.5, 1 and 1.5 $\mathrm{g\,l^{-1}}$. The particle Reynolds number was approximately 0.5 for all the discharges. The suspension criterion was evaluated by means of the ratio between the friction velocity and the settling velocity, computed as in Zanke (1977). The suspension criterion for all discharges exceeded 2.5, which means that suspended transport was dominant and that the sediment suspension over the whole water column is guaranteed (Yossef and de Vriend, 2010). The imposition of different initial sediment concentrations implies the release of different masses of sediments in the channel. However, this point is assumed and justified by the fact that the same probability is given to the sediments to be transported in suspension, i.e. the maximum sediment capacity concentration was imposed for each discharge.

Experiments were performed until reaching a quasi-equilibrium concentration state, i.e. 3, 4 and 5 h for the low, medium and high discharges, respectively. Equilibrium was assumed when the morphological changes in the lateral embayments were considered too small to be measured.

The concentration imposed at the beginning of the experiments in the channel decreased gradually, until it converged asymptotically to a lower final concentration. This decreasing evolution is due to the trapping by diverse elements of the physical system. In the reference case, a decaying concentration evolution is observed due to the sediment trapping within the base system: some of the particles are trapped in the small gaps between bricks and walls. These particles were removed after carrying out the experiments in order to avoid any bias in the results. The sediment concentration decay of the situations with lateral cavities was compared to the temporal evolution of the concentration in the reference situation (i.e. the reference channel without lateral embayments, geometric configurations 1.0, 2.0 and 3.0).

Experimental Techniques

2D surface particle image velocimetry (PIV)

The study of the flow pattern inside the cavities was performed using a 2D-surface PIV technique, as previously performed in Uijttewaal *et al.* (2001), Weitbrecht and Jirka (2001) and Uijttewaal (2014). Systematic photo sequences were taken on the same cavity for the three discharges and for all the configurations under steady flow conditions. A cavity in the centre of the channel was chosen that was representative of the flow pattern for all the other cavities; the chosen position was away from any effect from the upstream and downstream channel boundaries. Water levels were measured by means of ultrasonic probes with a frequency of 10 Hz. The accuracy of the water-level measurements was at least ± 0.002 m.

The PIV technique was applied by seeding the channel with floating polystyrene particles with a diameter of 3 mm and a density slightly below the density of the water (0.946). The photos were taken with a SUMIX SMX-160 camera placed horizontally above the cavity. The images were captured at a rate of 30 frames s^{-1} (30 Hz) at the beginning of the experiments, before the fine sediments were inserted into the flow. The acquisition time was several times higher than the *seiche* period estimated in Kimura and Hosoda (1997). This ensured that the measurements captured turbulence features well. These features, according to Kimura and Hosoda (1997), are generated at the shear layer with a period shorter than the period of the *seiche*.

The photo sequences were subsequently post-processed using the MATLAB package PIVLab (Thielicke and Stamhuis, 2014). The window deformation was corrected to track particles in the photo sequence. Each picture was divided into small sections for analysis, and a cross-correlation algorithm derived the most probable particle displacements. This generated an instantaneous velocity field between each pair of time steps. This information was then time averaged in order to analyse the stationary flow patterns present in the embayment. The Reynolds decomposition applied to the signal allowed the turbulence and shear stresses to be inferred.

The measurements obtained with the surface PIV only provide information concerning the motion of the free surface. Nevertheless, the shallowness of the configurations allows us to consider that the velocity field in the embayment is mainly 2D (Tuna *et al.*, 2013), and consequently the results can be used as a proxy to understand the phenomena occurring in the water column.

Suspended sediment monitoring

The temporal evolution of the suspended sediment concentration was recorded in two downstream locations in the channel: 3 m downstream the tranquillizer located at the channel entrance and 1 m upstream the gate at the final section of the channel. It was verified that these transitional lengths prevented any perturbation in the measurements by the upstream and downstream channel boundaries. Here, the suspended sediments were well dispersed within the flow.

The concentration acquisition system was composed of two Cosmos-25 turbidimeters. The turbidimeters were calibrated, and a linear relation was found between the tension in volts and the suspended sediment concentration. The linear regression for this analysis was statistically significant at the 95% confidence level, with correspondingly high coefficient of determination values, R^2 ($R^2 \geq 0.99$). The resulting sensitivity obtained for the turbidimeters was of the order of 0.5 $mg\,l^{-1}\,mV^{-1}$, and the range of the device was set between 0 and 6 V; i.e., the physical scale ranged between 0 and 3 $g\,l^{-1}$. Furthermore, the concentration data were sampled each 100 ms, and the signal was subsequently averaged over 25 time steps.

The information provided by the turbidimeters is punctual, and it corresponds to a value in the vertical concentration profile. It was experimentally checked that the chosen vertical position of the turbidimeter ensured that the measured values correspond roughly to the averaged concentration of the vertical profile. It was also verified that the chosen positions prevented the presence of air bubbles under the turbidimeters and possible signal reflection from the bottom, which could induce measurement errors.

Sediment deposition pattern

The study of the influence of the sedimentation on the cavity was performed following a twofold protocol: (i) plane view photos of the sedimentation patterns were taken at the end of the experiment and after slowly draining the channel in the same cavity where the PIV technique was applied. These photos were treated to extract the surface occupied by the sediments in order to cross-correlate their location with the information provided by the PIV technique. (ii) The total sediment mass trapped inside the lateral embayments was collected. Later, the sediment samples were dried in an oven to eliminate the water content and were then weighed. This mass was divided by the total area occupied by the embayments in order to compute the trapping efficiency for each configuration in mass per unit area, which is redundant information regarding the measurements of the temporal evolution of the sediment concentration.

Results

Water depth

The water level was measured over time for each configuration and compared with the reference channel where no lateral embayments existed. The results from the water measurements show that for the lowest discharge, 4.8 $l\,s^{-1}$, and the reference flow aspect ratio, $(b/h)_{ref} = 14.40–17.26$, the water level

decreased during the experiment for configurations where the cavity aspect ratio, AR, was lower and the expansion ratio, ER, was higher; that is, with respect to the reference channel, more space was allowed to the flowing water due the existence of the lateral expansion of the cross-section (geometric configurations 2.2, 2.3 and 3.1–3.4).

For the medium discharge, 8.5 $l\,s^{-1}$ and $(b/h)_{ref}$ = 10.08–12.08, the water level had steady characteristics. However, regarding the instantaneous signal, the water level was notably unstable, regardless of the configuration. This effect was more noticeable for medium cavity aspect ratios, AR = 0.4–0.5, and roughness aspect ratios, RR = 0.5–0.6. The imposed discharge in combination with the geometric design of the lateral embayments initiated an oscillation phenomenon in the channel corresponding to the above-referred *seiche*. The geometric configurations where the *seiche* phenomenon was more remarkable were 1.2, 2.2, 3.1, 3.2, 3.3 and 3.4. According to Akutina (2015), who used 3D-PTV techniques to study shallow embayment flows, seiching occurs when the frequency of the main recirculating pattern matches the natural frequency of the embayment determined by its geometry. Tuna *et al.* (2013) stated that the turbulence vortices created by the corners of the cavities excite the flow, leading to regular pulses in the flow. The phenomenon extended to the middle of the channel, where a small oscillation was observed (1–3 mm, depending on the configuration). It was assumed, nevertheless, that the velocity in the main channel remained practically constant, a fact that was later confirmed with the surface PIV results.

Finally, for the highest discharge, 15 $l\,s^{-1}$ and $(b/h)_{ref}$ = 7.20–8.63, the mean water level was increased in all the geometric configurations as a consequence of the increment of the *seiche*-type phenomenon.

Surface flow patterns

2D surface PIV results of the lateral cavities are presented in this subsection in a systematic way for all the geometric configurations and for all the discharges. Instantaneous (u, v), mean $(\bar{u}, \bar{v})$ and fluctuating (u', v') velocity fields were obtained, with u and v being the streamwise and spanwise velocities, respectively, measured at the water surface; see Franca and Brocchini (2015) for more details on the Reynolds decomposition of instantaneous turbulent signals. Bar ($\bar{}$) and prime ($'$) symbols stand for mean and fluctuating velocities, respectively. In addition to mean flow quantities, including time-averaged velocity and mean vorticity, defined as $\bar{\omega} = \frac{\partial \bar{v}}{\partial x} - \frac{\partial u}{\partial y}$, Reynolds shear stresses per water density, $\overline{u'v'}$, were calculated for the water surface plane. The algorithm used to estimate the spatial derivatives is based on the definition of vorticity proposed by Sveen and Cowen (2004). Negative vorticity represents flows rotating in the clockwise direction.

The results are available for the cavity and for the adjacent area of the main channel. A dimensionless scale was used to characterize the cavity geometry in the figures, where x/l denotes the longitudinal direction and y/l the transverse direction. l is the length of the cavity. Results for geometric configuration 2.1 are presented herein. The remaining results for all geometric configurations are provided as supplementary data (supporting information).

Figures 3 and S1–S9 display, for each geometric configuration, the following variables: (i) time-averaged streamwise velocity with the horizontal velocity vectors (top left); (ii) time-averaged spanwise velocity with the horizontal velocity vectors (top right); (iii) Reynolds shear stress with streamlines from the horizontal velocity field (bottom left); and (iv) mean vorticity with streamlines from the horizontal velocity field (bottom right). The results for the three different discharges, 4.8, 8.5 and 15 $l\,s^{-1}$, correspond respectively to the reference shallowness ratios of b/h = 14.40–17.26, 10.08–12.08 and 7.20–8.63, which are plotted from top to bottom. The shaded area indicates the region where the sediments settled at the end of the experiment. In the dashed areas, information was not available to perform the PIV estimation of the velocity. The streamwise velocity of the channel in the reference configuration was subtracted from the streamwise velocity field in the main channel region for all the geometric configurations tested. It was meant to highlight the impact of the cavities in the flow patterns. No velocity was subtracted in the spanwise direction, since the flow in the main channel in the reference configuration was mainly 1D, and consequently the lateral velocity was negligible.

Depending on the geometric ratios of the lateral embayments, the flow is characterized by the formation of one or more large-scale vortical structures that totally or partially fit the cavity area. Nevertheless, in all geometric configurations and in all the flows, a main clockwise recirculating system (composed of a so-called main recirculating eddy) is observed in the streamlines plot, with a clear imprint in the distribution of the mean longitudinal and transversal velocity fields. This is located in the downstream part of the cavity; i.e., the position of the centre of this vortical structure is always after x/l =0.5.

This main recirculating eddy has its origin in the flow separation generated by the sudden widening upstream imposed by the cavity. The flow separation diverts the flow from the main channel towards the cavity. This flow, in turn, is confined by the downstream wall of the cavity, imposing its recirculation. A velocity plume, associated with the vortical structure when the flow leaves the cavity and re-enters the main flow, is clearly observed in the streamwise velocity field for all the tests.

Outside of the lateral embayment, the flow is unidimensional, following the main direction of the channel. The influence of the cavities in the main channel flow is always confined to a distance of less than l from the wall roughness elements.

Regarding the distribution of the Reynolds shear stress ($\overline{u'v'}$), the highest values typically appear in the mixing layer area, i.e. the region where the momentum exchange between the main flow and the lateral embayment takes place. Two trends are observed when comparing the results: for geometric configurations 2.1 and 3.2–3.3, with high cavity aspect and expansion ratios, the magnitude of the shear stress increases with the discharge (see, for example, configuration 2.1, Figure 3). For configurations with a low expansion ratio, ER, and a low cavity aspect ratio, AR, the higher discharges do not imply higher shear stress values (see, for example, configuration 1.3, Figure S3).

The vorticity represented in Figure 3 corresponds to a spatial discretization of the data corresponding to the camera resolution. The maximum vorticity is generally associated with three regions of the flow: the centre of the main recirculating eddy, the inner cavity walls (y/l = 0; x/l = 0; x/l = 1) and the shear layer (maximal y/l). The vorticity observed in the centre of the main recirculating eddy is negative, and it follows the sense and direction of the in-cavity recirculating flow. The positive vorticity observed in the inner cavity walls is caused by the shear between the inner walls and the main recirculating eddy. In the shear layer, a positive vorticity is mainly found as a result of the shear between the flow of the main channel and the outflow of the cavity. Generally, but not exclusively, an increase in discharge implies an increase in the mean

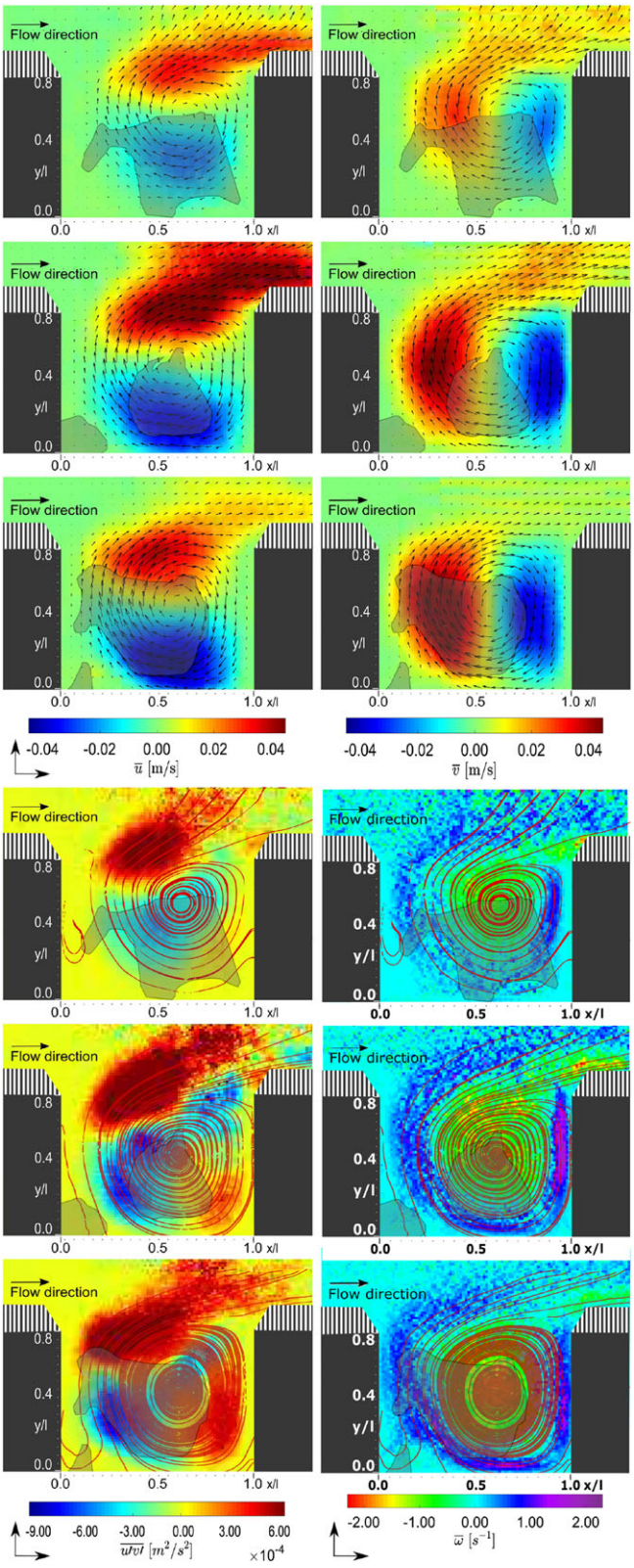

Figure 3. Geometric configuration 2.1 (see Table I). Time-averaged streamwise velocity with the velocity vectors (top left); time-averaged spanwise velocity with the velocity vectors (top right); Reynolds shear stress with a few streamlines (bottom left) and mean vorticity with a few streamlines (bottom right). The results plotted from top to bottom correspond to discharges of 4.8, 8.5 and 15 $l\,s^{-1}$. Shaded areas indicate the region where the sediments settled at the end of the experiment, when equilibrium conditions are reached. In the dashed area information was not available for performing the PIV computations. The streamwise velocity of the channel in the reference configuration was subtracted from the streamwise velocity field in the area of the main channel. [Colour figure can be viewed at wileyonlinelibrary.com]

vorticity (see geometric configurations 1.1, 2.2, 3.1, and 3.2 in Figures S1, S4, S6 and S7, respectively).

The sediment deposition and the surface flow patterns can also be cross-analysed in Figures S1–S9. The main vortex identified earlier typically corresponds to an area of sediment deposition in the embayment. High positive longitudinal velocity areas match the absence of sedimentation close to the main flow interface, corresponding to the area of influence of the detached eddies coming from the upstream corner of the cavity. In addition, a dead area starting from the inner upstream corner ($x/l = 0$ and the maximum of y/l) to the middle of the length of the cavity ($x/l \approx 0.5$) may be found in some configurations, corresponding to areas where the sediments accumulate (Figure S4). Reynolds shear stress and vorticity may also be used as indicators of the position where sedimentation is taking place. Areas with high positive shear stress correspond to regions where strong mass exchange occurs, i.e. more sediments flowing into the cavities, so a higher presence of sediment is expected there. Furthermore, negative vorticity in the centre of the eddies contributes to trapped and downwelled sediments inside the cavities.

Sediment concentration

During the experiments, the sediment concentration was recorded at two streamwise positions within the channel (cf. Figure 2). The averaged value of both measurements is herein analysed. Since the experiments were performed with different discharges, the capacity sediment concentrations initially imposed were different for each of the three discharges. The concentration results were normalized by this initial concentration.

For the sake of conciseness in this section, only the results belonging to geometric configurations of group 3 are presented. The remaining results are provided as supplementary data (supporting information). The left-hand panel of Figures S10, S11 and 4 display for each geometric configuration the time decay for the normalized sediment concentration. The results from top to bottom correspond respectively to discharges of 4.8, 7.5 and 15 $\mathrm{l\,s^{-1}}$. The experimental data were fitted by means of an exponential-type equation: $f(t) = a + b \cdot \exp(c \cdot t)$. The exponential regressions for this analysis were statistically significant at the 95% confidence level, with correspondingly high R^2 values ($R^2 \geq 0.90$). Parameters of the exponential fits are displayed in Tables S1–S3. The results of the reference experiments, corresponding to the measurements made with prismatic reference configurations 1.0, 2.0 and 3.0, are plotted in black.

Except for geometric configuration 3.4 at medium discharge, the sediment concentration of the reference test is always above the sediment concentration of the other geometric configurations. Configuration 3.4 is an extreme situation of lateral embayments, with a high roughness ratio (RR) and high cavity density (CD) (it resembles more a groyne field), and large differences in the results for this configuration are observed with regard to the other configurations.

The time evolution of the concentration is similar, regardless of discharges and geometric configurations. At the beginning, the sediment concentration drops rapidly, then stabilizes, and finally it converges asymptotically towards a quasi-equilibrium. For some experiments, i.e. geometric configurations 1.1 and 1.3 at medium discharge, the equilibrium is still not fully achieved, but it was decided to keep the same time duration for all the runs in order to make them

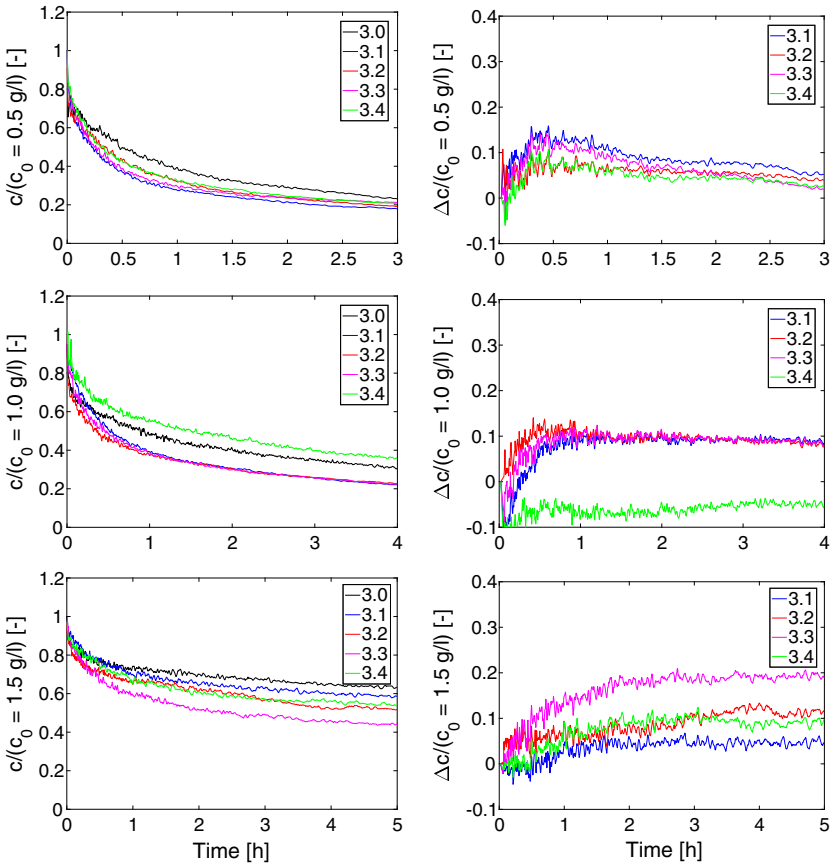

Figure 4. Geometric configurations of group 3 (see Table I). Time evolution of the normalized sediment concentration, c/c_0. The curves are normalized by the initial concentration (left). Time evolution of the difference between the sediment concentration of each configuration and the sediment concentration of the reference test, $\Delta c/c_0$. The curves are normalized by the initial concentration (right). Results plotted from top to bottom correspond to discharges of 4.8, 8.5 and 15 $\mathrm{l\,s^{-1}}$, respectively. [Colour figure can be viewed at wileyonlinelibrary.com]

comparable. Furthermore, it is observed that the decay in sediment concentration is faster for lower discharges. Higher discharges increase turbulence levels, and consequently they increase sediment suspension. Therefore, the equilibrium concentration at the end of the experiments is always lower for the lowest discharge.

The right-hand panels of Figures S10, S11 and 4 display the time evolution of the normalized difference between the sediment concentration for the reference case (c_{ref}) and the sediment concentration for each configuration (c_{conf}), $\Delta c/c_0$, being $\Delta c = c_{ref} - c_{conf}$. The empirical curves are normalized by the initial concentration for each discharge.

The curves of the normalized difference show a different behaviour among configurations. Most of the curves present a rising limb at the beginning of the experiment (due to the initial sediment trapping) and, subsequently, a falling limb that reaches an equilibrium stage. For the geometric configurations of group 1 with the medium discharge, for configuration 1.2 with the highest discharge and for configurations of group 3 with the highest discharge, the trend of the curve is different. Nevertheless, the concentration difference increases all along the experiment. For the three geometric groups, the highest difference in the $\Delta c/c_0$ at the end of the experiment is obtained with the medium discharge.

Sediments trapped in the lateral embayments

The sediment mass trapped inside the lateral embayments, after equilibrium conditions are met, was collected, dried and weighed. The mass was divided by the total area occupied by the lateral embayments in order to compute the trapping efficiency for each configuration. Figure 5 displays this trapping efficiency for all the geometric configurations considered in the three groups. Additionally, superimposed grey patches depict the trapping efficiency calculated by means of the integration of the difference between the sediment concentration decay and the initial sediment concentration of each configuration. The trapped mass computed by this second method provides systematically higher values for the three groups. For groups 1 and 2, the mismatch between mass collected and integrated is higher. Nevertheless, it is shown that, regardless of the method considered for computing the trapped mass, the trend in the sediment trapping among discharges for each geometric configuration is the same.

Comparing among the three groups, we find the following: (i) group 2 reaches the highest trapping efficiency; (ii) group 1 presents medium efficiency; and (iii) group 3 achieves the lowest efficiency. For group 3, the sediments trapped in the lateral embayments are approximately four times less than for group 2 or group 1.

On the other hand, the trapping effectiveness variation with respect to the three different discharges shows a common distribution with the different configurations: the flow with the medium discharge normally traps more sediments than the low or high discharge. This means that the hydrodynamic conditions inside the cavity for this discharge favour settling of the sediment. For the low discharge, small differences are observed among the different geometric configurations.

Regarding the geometric ratios, the highest cavity aspect ratio, AR = 0.8, corresponds to the lowest trapping efficiency when compared with geometric configurations within the same group. Furthermore, an increase in RR leads to a decrease of the trapping efficiency (see the different geometric configurations within group 3).

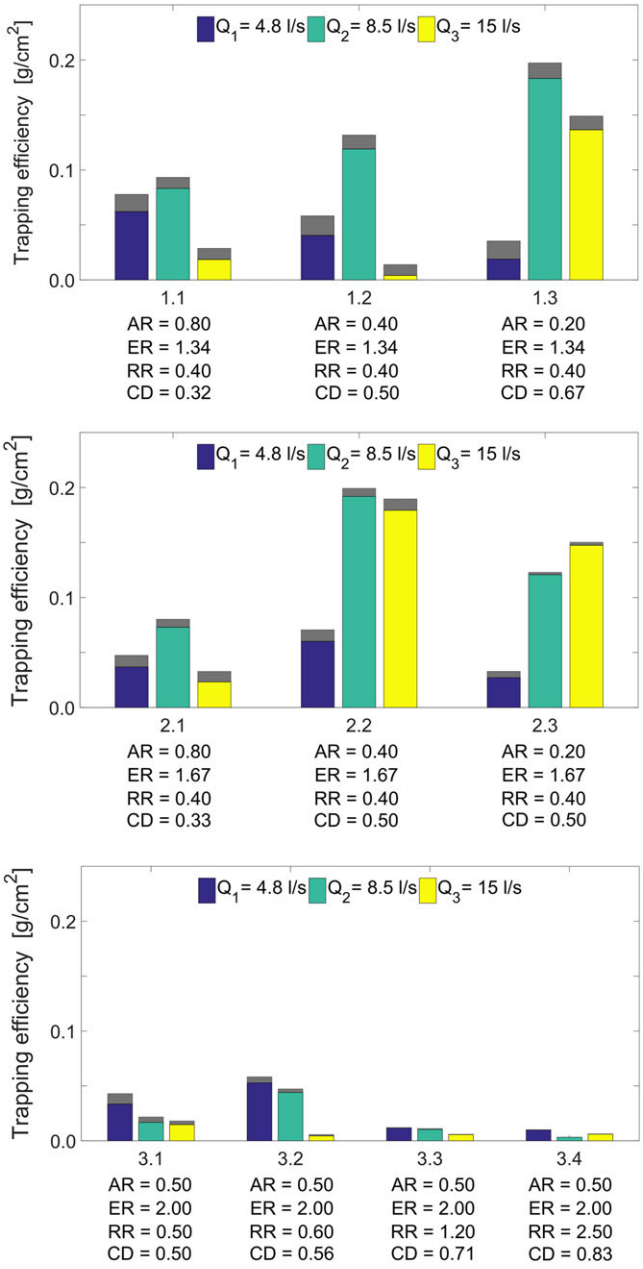

Figure 5. Trapping efficiency for all the geometric configurations contained in the three groups. Grey patches depict the trapping efficiency computed with the temporal integration of the sediment concentration measurements. [Colour figure can be viewed at wileyonlinelibrary.com]

Discussion

Flow and sedimentation patterns

Depending on the geometry of the lateral embayments, the flow is characterized by the formation of one or more large-scale vortical structures that can occupy part of or the whole embayment. The main recirculating eddy is responsible for the sediment entrainment and eventual settling into the lateral embayments. The more intricate the flow pattern inside the cavity (which can be inferred by the length of the streamlines), the longer the path that the trapped sediments have to wind inside the cavity. Longer paths within the cavity correspond to larger residence time of the sediment in the cavity, i.e. a higher probability for the sediment to be settled.

The cavity aspect ratio, AR = W/l, and the cavity density, CD, of the lateral embayments are the determinant parameters for the location and number of eddies inside the cavities. If the distance between the inner upstream and downstream walls is small, CD = $l/(l+L) < 0.5$ (see geometric configurations 1.1 and 2.1 in Figures S1 and 3), the flow separation occurring at the edge of the upstream wall will not reattach to the inner lateral wall. Hence, when CD = $l/(l+L) \geq 0.5$ (see the rest of the geometric configurations in Figures S2–S9, the flow separation intercepts the downstream macro-roughness element. The protruding elements work as an ensemble as a continuous rough wall, and the flow is of the skimming type. When the distance between the inner upstream ($x/l = 0$) and downstream ($x/l = 1$) walls is large, the flow separated upstream reattaches to the inner lateral wall of the cavity ($y/l = 0$), and the macro-rough elements can be considered as lateral singularities in the channel flow.

Figure 6 presents the relation between the normalized longitudinal coordinate (x/l) of the centre of the main recirculating eddy inside the embayment and the cavity aspect ratio, AR. When the cavity aspect ratio, AR = W/l, tends to unity, the cavity tends to a square shape. In this case, a single eddy is formed inside the cavity occupying the whole cavity, as seen by Mignot *et al.* (2016). For AR = 0.8, geometric configurations 1.1 and 2.1, a quasi-circular eddy appears inside the cavity, and the centre of the vortex is found near the centre of the cavity ($x/l \approx 0.5$). For lower cavity aspect ratio values, the centre of the vortex moves systematically towards the inner downstream wall ($x/l \approx 1.0$). The combination of low cavity aspect ratios, AR = 0.2–0.4, with high cavity density values, CD = $l/(l+L) \geq 0.5$, leads to the formation of secondary eddies for the high and, occasionally, for the medium discharge: geometric configurations 1.3, 2.2, 2.3 and 3.4 (cf. Figures S3, S4, S5 and S9). The red outline symbols depict experiments where a secondary eddy was also formed. The secondary eddy rotates with less intensity than the primary eddy, as stated in previous studies on flow recirculation and mass exchange in groyne fields (Uijttewaal *et al.*, 2001; Weitbrecht *et al.*, 2007; Uijttewaal, 2014).

The expansion ratio, ER, which quantifies the degree of channel widening introduced by the cavity in the central channel, has an impact on the sedimentation process. Focusing on the group of tests 1 and 2, with a constant ER, the cavity aspect ratio, AR, seems to have an influence on the sedimentation, mainly for the medium and high discharges. The higher the expansion ratio and the smaller the cavity aspect ratio, the larger are the dead areas (regions with low recirculating velocities, previously described by Kimura and Hosoda, 1997). Of the geometric configurations of groups 1 and 2, 2.3 (ER = 1.67, AR = 0.2) presents the largest dead areas; see Figure S5. These dead areas impose higher residence times on the suspended sediments, thus favouring sedimentation. This sedimentation occurs mainly in the upstream region of the embayments, $x/l \approx 0$. Nonetheless, it is important to recall that dead areas are not the only factors responsible for sedimentation. The mass exchange between the main channel and the cavity (observed, for example, in the spanwise velocity fields) also favours the in-cavity circulation of sediments, and it thus increases the potential for sedimentation. Therefore, although geometric configuration 2.3 presents the largest dead areas, it does not have the largest sediment trapping efficiency within geometric group 2 (see Figure 5).

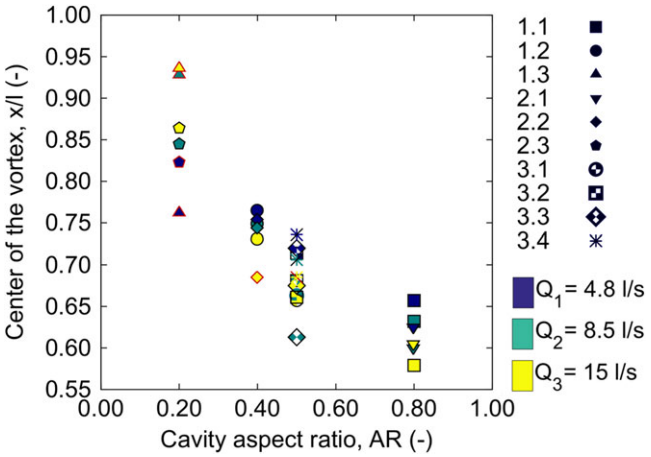

Figure 6. Normalized longitudinal coordinate (x/l) of the centre of the main recirculating eddy inside the embayment for all the geometric configurations and as a function of the cavity aspect ratio, AR. Red-outlined symbols represent experiments where a secondary eddy was observed. [Colour figure can be viewed at wileyonlinelibrary.com]

Among the geometric configurations of groups 1 and 2, 2.3 (ER = 1.67, AR = 0.2) presents the largest dead areas; see Figure S5. These dead areas impose higher residence times on the suspended sediments, thus favouring sedimentation. This sedimentation occurs mainly in the upstream region of the embayments, $x/l \approx 0$.

When the aspect and roughness aspect ratios are low (AR = 0.2, RR = 0.4), regions with maximum magnitude of shear stresses and vorticity are larger for the low and medium discharges than for the high discharge (Figure S2). This result for these geometric configurations (AR = 0.2, RR = 0.4) is related to the presence of the *seiche*, which homogenizes small-scale fluctuations in the flow; in exchange, this promotes vertical mixing, hindering the sediment from settling. The higher the relevance of the *seiche* in the flow (cf. the highest discharge), the lower are the observed shear instabilities, leading to a reduced vorticity production (Balmforth (1999); Kolyshkin and Ghidaoui (2002); Akutina (2015). This results in a longer residence time of the sediments and thus a higher sediment trapping in the cavities for low and medium discharges. The *seiche* leaves a footprint in the total amount of sediment trapped in the lateral embayment, as observed in the results obtained for the sediment trap efficiency: the medium discharge (not the highest discharge) is the one that generally traps the largest amount of sediments inside the lateral embayment.

When comparing the sedimentation patterns with the surface PIV results, it is observed that the main vortex found in the lateral embayment corresponds generally well with the main area of sediment deposition. However, the superficial area of the main vortex is larger than the area where the sediments are deposited. In general, particles seem to flow into the core region of the main recirculating eddy and settle there. A *tea-cup* effect may thus be observed (visual observation): the main vortex causes the appearance of secondary eddies created by its own rotation. Recent studies (Tuna *et al.*, 2013; Akutina, 2015) theorize that these secondary eddies drag the sediments towards the centre of the vortex, where they subsequently settle down. The findings herein provided confirm this theory.

Time evolution of the sediment concentration

The left-hand panel of Figure 7 displays the normalized sediment concentration decay during the first hour as a function of the cavity aspect ratio, AR, for all the geometric configurations. The decay values are computed by means of the

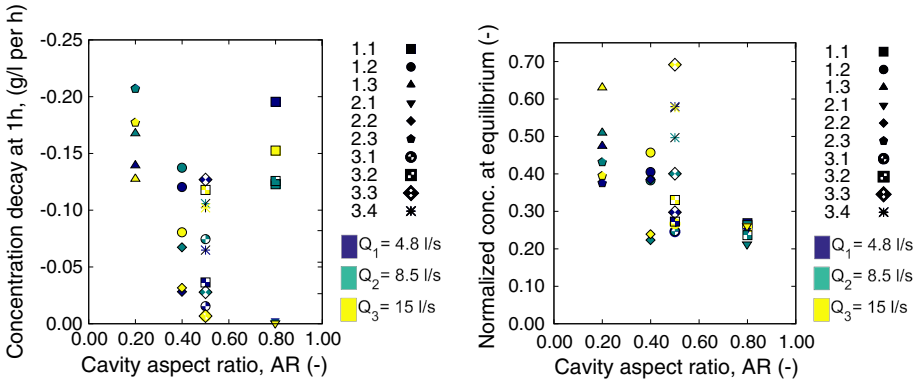

Figure 7. Sediment concentration decay during the first hour as a function of the cavity aspect ratio, AR, for all geometric configurations (left). Normalized concentration values at equilibrium as a function of AR for all geometric configurations (right). [Colour figure can be viewed at wileyonlinelibrary.com]

exponential fits presented in Section 1, since the data are well represented by such a fit. For low and medium discharges, and regardless of the geometric configuration considered, the drop in the sediment concentration is larger than for the highest discharge. Thus the normalized equilibrium concentration at the equilibrium (right-hand panel of Figure 7) is lower for the low and medium discharges. This can be explained by the lower velocities and, consequently, less turbulence in the flow, which is responsible for keeping the sediments in suspension (see the Rouse number in Table II). Also, the reduced settling velocity of the sediment, which, for high suspended sediment concentrations (above 1 $g\,l^{-1}$) is caused by the interactions among particles, decreases the settling velocity with increasing sediment concentration (Mehta and McAnally, 2007). The higher drop in the sediment concentration for the low and medium discharges (i.e. in-cavity sediment deposition) is generally reflected in the higher trapping efficiency for these low (see Figure 5 for geometric configurations 3.1 and 3.2) and medium (see Figure 5 for geometric configurations 1.1, 1.2, 1.3, 2.1, 2.2) discharges.

Conversely, lower values of the cavity aspect ratio, AR = 0.2–0.5, seem to be related to a quicker drop in sediment concentration (see Figure 7, left-hand panel). Configuration 1.1 departs from this trend, showing high-concentration decays despite having an AR = 0.8. However, this is explained by the flow patterns associated with its lowest cavity density ratio, CD = 0.32, and by its lowest expansion ratio, ER = 1.34: more intricate streamlines inside the cavity favour the sedimentation (see Figure S1). Furthermore, regarding the normalized concentration at the equilibrium (see Figure 7, right-hand panel), it is also observed that higher cavity aspect ratios, AR, lead to lower-equilibrium sediment concentrations. It is thus concluded that lower values of the cavity aspect ratio, AR = 0.2–0.5, display a quicker sediment trapping at the beginning of the experiments, and once the cavity is partially filled with sediment the sediment concentration maintains a stable value. In other words, the in-cavity morphodynamic equilibrium is reached more quickly and it is preserved without alterations until the end of the experiments.

From the left-hand panels of Figures S10, S11 and 4, the roughness ratio and cavity density seem to be indirectly related to the concentration. The increase of these two means an increase in the turbulence levels in the flow, which favours the suspension of sediments.

Moreover, the largest differences between the sediment concentration of each configuration and the reference configuration are observed for the medium discharge (the effect of the *seiche* is weaker for this discharge, so less vertical mixing is promoted). Generally, the curve presents a rising limb followed by a plateau that remains constant when equilibrium conditions are met. The rising limb corresponds to the initial sediment trapping until a new equilibrium capacity situation is reached. The equilibrium values (last values in the graphs from Figures 4 to S10–S11), correspond to the net trapped sediment difference between the prismatic channel and the channel with imposed lateral cavities. When the equilibrium value is (or tends to) zero, the insertion of the cavities in the channel does not change the transport capacity of the flow (i.e. the in-cavity sediment trapping stops, since the morphological equilibrium is reached). After the first impact observed in the concentration curves due to the sediment retention in the cavities, the concentration returns to values equivalent to the reference situation (prismatic channel). This happens mainly for low discharges, when the levels of turbulence in the flow are lower.

For test 3.4 (with a geometric configuration equivalent to a groyne field) with the medium discharge, this net difference is negative, indicating that this combination promotes more sediment suspension than in the reference test. This is one of the main reasons for the construction of groyne fields in river channels: increased sediment transport capacity in the central part of the channel for avoiding deposition. Previous studies have stated that the flow characteristics are completely different between isolated cavities and groyne fields (Uijttewaal *et al.*, 2001; Weitbrecht and Jirka, 2001; Rivière *et al.*, 2010). In the groyne field, the lateral embayments work as an ensemble, and the turbulent vortices formed in the corners of the groynes prevent sedimentation inside the cavities (McCoy *et al.*, 2008).

Sediment trapping efficiency

A higher trapping efficiency is observed for the medium discharge. With respect to the low discharge, the trapping efficiency can be explained by the fact that the increase in discharge induced a more complex flow pattern, where the residence time of the sediments in the cavity increased, inducing sedimentation. However, with respect to the high discharge, this argument is not valid. The *seiche* is responsible for these results, since it promotes vertical mixing and sediment resuspension. This statement is supported by the results in Figure 8. This presents the trapping efficiency of all the geometric configurations as a function of the ratio of the energy losses due to the *seiche* phenomenon relative to the total energy dissipation. The *seiche* losses here are taken as a surrogate of the *seiche* strength. They were computed as in Meile *et al.* (2011b) by means of the ratio between the

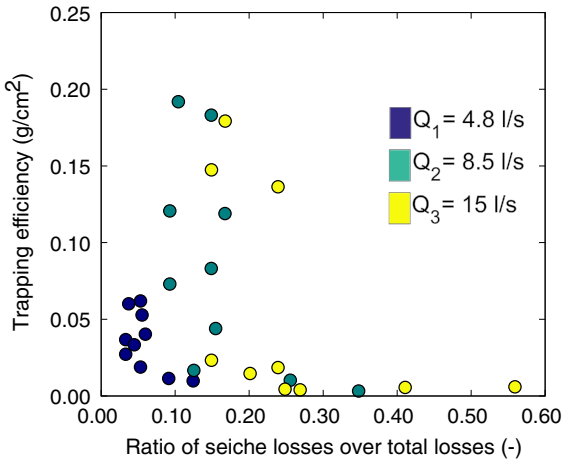

Figure 8. Trapping efficiency for all the geometric configurations as a function of the ratio of the *seiche* losses over the total losses. [Colour figure can be viewed at wileyonlinelibrary.com]

potential energy of the point with maximum water height (i.e. a point inside the embayment impacted by the *seiche*) and the potential energy of the corresponding horizontal water surface level (i.e. a point in the middle of the channel). As was noted in Meile *et al.* (2011b), this is an upper limit of the *seiche* losses, since it is assumed that there is no friction loss in the transverse direction (i.e. from the middle of the channel to the inner points of the embayments). Furthermore, the total energy dissipated in the length of $L + l$ (i.e. the cavity and its neighbouring channel bank) is calculated as a contribution of the friction and form drag Meile *et al.* (2011b). The increasing discharge is proportional to the greater energy losses dissipated by the *seiche*. Larger amounts of sediment are trapped inside the embayments for the low discharge and, particularly, the medium discharge. In contrast, the highest discharge with larger *seiche* losses (and thus higher *seiche* strength) presents the lowest trapping efficiency. As described in Section 1, the *seiche* homogenizes the small-scale fluctuations in the flow and promotes vertical mixing, preventing the sediments from settling.

Focusing on the geometry of the embayments, the cavity aspect ratio AR and, inversely, the cavity density, CD, show the most significant impact on the trapping efficiency. Embayments with a cavity aspect ratio of AR = 0.8 trap considerably less sediment than embayments with a lower AR. This increase of mass exchange with a decreasing AR is confirmed by former studies on mass exchange in groyne fields (Uijttewaal *et al.*, 2001; Weitbrecht and Jirka, 2001). Another argument that highlights the relevance of this geometric ratio is the small difference among values found in the geometric configurations of group 3. For this group, the cavity aspect ratio is kept constant for all the tests. However, a reduction in sediment trapping is observed when the cavity density increases, CD > 0.50 (with the exception of geometrical configuration 3.2).

The trapping efficiency tends to increase with ER. This is observed when comparing groups 1 and 2, where only the ER is changed. The increased trapping efficiency can be explained by the increase in the area for the mass exchange, where lower flow velocities and levels of turbulence are established. The experiments in group 3 exhibit an even higher ER. However, they do not show a higher trapping efficiency. This can be explained by the increased RR, which is counteracting the effect of the ER.

The influence of RR and of CD on the trapping efficiency is more evident. With an increase in both ratios (cf. results for group 3, RR > 0.50 and CD > 0.50), the trapping efficiency is significantly reduced. This can be explained by the increased turbulence in the channel that is induced due to the increased roughness. Therefore, particles are more easily kept in suspension and settling is hindered. In contrast, for low cavity density values (CD < 0.50, geometric configurations 1.1 and 2.1), the recirculating flow type observed in the cavities belongs to the skimming flow type (Meile *et al.*, 2011a). This implies that the flow in the cavities is largely decoupled from the main channel. Hence the mass and momentum exchange between the cavity and the main channel are limited, and so is the amount of sediment trapped in the embayment.

Conclusions

Here, the influence of side macro-rough elements in the transport of sediments by suspension was analysed experimentally using four main techniques: surface PIV, images, concentration measurements in time and weighing of trapped sediments. These techniques allowed analysis of the flow in terms of hydrodynamics, sediment transport and morphodynamics. Different geometries, three discharges and different initial concentrations were varied.

A strong relation between the flow hydrodynamics of the lateral cavities and the sediment dynamics was observed. A main vortical structure, which may be associated with a more or less complex flow structure depending on the geometry characteristics of the cavity, was identified and shown to correspond to a sediment settling area. Sheltered areas within the cavity, identified in terms of flow streamlines, generally correspond to areas where sediment settles.

The analysis of different geometries combined with three different discharges that correspond to different flow aspect ratios shows that, in general, complex and intricate flow patterns favour deposition. This happens because these factors will impose longer residence times inside the cavity on the sediments captured inside. The longer the sediments remain in the cavity, where the turbulence levels are lower than in the main channel, the higher the probability of settling. Consequently, configurations with a lower cavity aspect ratio, AR = W/l, correspond to higher sedimentation.

Generally, lower sedimentation is observed for configurations corresponding to higher roughness, RR = W/L, and cavity density ratios, CD = $l/(l + L)$. These introduce higher turbulence levels in the channel, which favours suspension. Looking at the whole set of geometric ratios, the lateral embayments with a high aspect ratio, high expansion ratio and low roughness aspect ratio, RR = W/L, are filled up faster. Conversely, lateral embayments with large aspect and roughness aspect ratios and a low expansion ratio are filled up only partially and slowly.

The discharge also plays an important role in the sediment trapping by the cavities. The highest trapped mass normally corresponds to the medium discharge. When compared to the low discharge, this is justifiable because the capacity transport of the channel in higher discharges corresponds to higher concentrations and thus more available sediment. However, in the case of the highest discharge, the *seiche* appears inside the cavities, which homogenizes the small-scale fluctuations in the flow and promotes vertical mixing, hindering sediments from settling.

Acknowledgements— This work was funded by the ITN-Programme (Marie Curie Actions) of the European Union's Seventh Framework Programme FP7-PEOPLE-2013-ITN, under the REA grant agreement n_607394-*SEDITRANS*, and by the FOEN (Federal Office for the

Environment, Switzerland) within the framework of the research project *Sediment and Habitat Dynamics*.

References

Abad J, Rhoads B, Guneralp I, García M. 2008. Flow structure at different stages in a meander-bend with bendway weirs. *Journal of Hydraulic Research* **134**: 1052–1063.

Akutina Y. 2015. *Experimental investigation of flow structures in a shallow embayment using 3D-PTV*. PhD thesis, McGill University, Montreal.

Allan JD, Castillo M. 2007. *Stream Ecology: Structure and Function of Running Waters*. Springer: Berlin.

Balmforth N. 1999. Shear instability in shallow water. *Journal of Fluid Mechanics* **387**: 97–127.

Baxter CV, Hauer FR. 2000. Geomorphology, hyporheic exchange, and selection of spawning habitat by bull trout (Salvelinus confluentus). *Canadian Journal of Fisheries and Aquatic Sciences* **57**: 1470–1481.

de Vries M. Use of Models for River Problems: Prepared for the International Hydrological Programme within Project M-3-5(a) (IHP-IV), Studies and Reports in Hydrology Paris, 1993.

Federal Office for the Environment. 2016. Hydrological Data Service for watercourses and lakes. [1. September 2016] http://www.bafu.admin.ch/wasser.

Franca MJ, Brocchini M. 2015. Turbulence in rivers. In *Rivers: Physical, Fluvial and Environmental Processes*, Rowinski P, Radecki-Pawlik A (eds), Springer: Berlin; 51–78.

Henning M, Hentschel B. 2013. Sedimentation and flow patterns induced by regular and modified groynes on the River Elbe, Germany. *Ecohydrology* **6**: 598–610.

Hinterberger C, Frohlich J, Rodi W. 2007. Three-dimensional and depth averaged large-eddy simulations of some shallow water flows. *Journal of Hydraulic Engineering* **133**: 857–872.

Hudson H. 2002. *Development of an In-Channel Coarse Sediment Trap Best Management Practice. Report*. Environmental Management Associates: Kenilworth, UK.

Imran J, Khan SM, Pirmez C, Parker G. 2017. Froude scaling limitations in modeling of turbidity currents. *Environmental Fluid Mechanics* **17**: 159–186.

Kemp P, Sear D, Collins A, Naden P, Jones I. 2011. The impacts of fine sediment on riverine fish. *Hydrological Processes* **25**: 1800–1821.

Kimura I, Hosoda T. 1997. Fundamental properties of flows in open channels with dead zone. *Journal of Hydraulic Engineering* **123**: 98–107.

Klosch M, Habersack H. 2017. The hydromorphological evaluation tool (HYMET). *Geomorphology* **291**: 143–158.

Kolyshkin A, Ghidaoui M. 2002. Gravitational and shear instabilities in compound and composite channels. *Journal of Hydraulic Engineering* **128**: 1076–1086.

Kondolf G. 1997. Hungry water: Effects of dams and gravel mining on river channels. *Environmental Management* **21**: 533–551.

Langendoen E, Kranenburg C, Booij R. 1994. Flow patterns and exchange of matter in tidal harbours. *Journal of Hydraulic Research* **32**: 259–270.

Lawrence DSL. 1997. Macroscale surface roughness and frictional resistance in overland flow. *Earth Surface Processes and Landforms* **22**: 365–382.

Le Coz J, Brevis W, Niño Y, Paquier A, Rivière N. 2006. Open channel side-cavities: A comparison of field and flume experiments. *River Flow* **1**: 145–152.

McCartney M. 2009. Living with dams: Managing the environmental impacts. *Water Policy* **11**: 121–139.

McCoy A, Constantinescu G, Weber L. 2008. Numerical investigation of flow hydrodynamics in a channel with a series of groynes. *Journal of Hydraulic Engineering* **134**: 157–172.

Mehta AJ, McAnally WH. 2007. Fine-grained sediment transport. In *Sedimentation Engineering: Processes, Measurements, Modeling and Practice*, Garcia M (ed), Manuals of Practice 110. ASCE: Reston, VA; 267–274.

Meile T, Boillat J, Schleiss AJ. 2011a. Flow resistance caused by large-scale bank roughness in a channel. *Journal of Hydraulic Engineering* **137**: 1588–1597.

Meile T, Boillat J, Schleiss AJ. 2011b. Water-surface oscillations in channels with axi-symmetric cavities. *Journal of Hydraulic Research* **49**: 73–81.

Mignot E, Cai W, Launay G, Rivière N, Escauriaza C. 2016. Coherent turbulent structures at the mixing-interface of a square open-channel lateral cavity. *Physics of Fluids* **28**: 045104.

Mignot E, Cai W, Polanco JI, Escauriaza C, Riviere N. 2017. Measurement of mass exchange processes and coefficients in a simplified open-channel lateral cavity connected to a main stream. *Environmental Fluid Mechanics* **17**: 429–448.

Morris M. 1955. A new concept of flow in rough conduits. *Transactions of the American Society of Civil Engineers* **120**: 373–410.

Nezu I, Onitsuka K. 2002. PIV measurements of side-cavity open-channel flows: Wando model in rivers. *Journal of Visualization* **5**: 77–84.

Ribi J-M, Boillat J-L, Peter A, Schleiss AJ. 2014. Attractiveness of a lateral shelter in a channel as a refuge for juvenile brown trout during hydropeaking. *Aquatic Sciences* **76**: 527–541.

Rivière N, Garcia M, Mignot E, Travin G. 2010. Characteristics of the recirculation cell pattern in a lateral cavity. In *River Flow*, Vol. 2010, Bundesanstalt für Wasserbau: Karlsruhe, Germany; 250–258.

Sanjou M, Nezu I. 2013. Hydrodynamic characteristics and related mass transfer properties in open-channel flows with rectangular embayment zone. *Environmental Fluid Mechanics* **13**: 527–555.

Sternecker K, Wild R, Geist J. 2013. Effects of substratum restoration on salmonid habitat quality in a subalpine stream. *Environmental Biology of Fishes* **96**: 1341–1351.

Sukhodolov A. 2014. Hydrodynamics of groyne fields in a straight river reach: Insight from field experiments. *Journal of Hydraulic Research* **52**: 105–120.

Sukhodolov A, Uijttewaal W, Engelhardt C. 2002. On the correspondence between morphological and hydrodynamical patterns of groyne fields. *Earth Surface Processes and Landforms* **27**: 289–305.

Sveen J, Cowen E. 2004. Quantitative imaging techniques and their application to wavy flows. In *PIV and Water Waves*, Grue J, Liu PL-F, Pedersen GK (eds), World Scientific: Singapore; 1–49.

Ten Brinke W, Schulze F, Van Der Veer P. 2004. Sand exchange between groyne-field beaches and the navigation channel of the Dutch Rhine: The impact of navigation versus river flow. *River Research and Applications* **20**: 899–928.

Thielicke W, Stamhuis E. 2014. PIVlab: Towards user-friendly, affordable and accurate digital particle image velocimetry in MATLAB. *Journal of Open Research Software* **2**: e30.

Tuna B, Tinar E, Rockwell D. 2013. Shallow flow past a cavity: Globally coupled oscillations as a function of depth. *Experiments and Fluids* **54**: 1586.

Uijttewaal W. 2014. Hydrodynamics of shallow flows: Application to rivers. *Journal of Hydraulic Research* **52**: 157–172.

Uijttewaal WSJ, Lehmann DV, Mazijk AV. 2001. Exchange processes between a river and its groyne fields: Model experiments. *Journal of Hydraulic Engineering* **127**: 928–936.

Uno K, Kazuuma N, Tsujimoto G, Kakinoki T. 2013. Trapping effect of fine sediment in wand. *Journal of Japan Society of Civil Engineers, Series B3* **69**: 922–927.

Van Rijn L. 2007. Unified view of sediment transport by currents and waves. I. Initiation of motion, bed roughness, and bed-load transport. *Journal of Hydraulic Engineering* **133**: 649–667.

Van Schijndel SA, Kranenburg C. 1998. Reducing the siltation of a river harbour. *Journal of Hydraulic Research* **36**: 803–814.

Von Bertrab M, Krein A, Stendera S, Thielen F, Hering D. 2013. Is fine sediment deposition a main driver for the composition of benthic macroinvertebrate assemblages *Ecological Indicators* **24**: 589–598.

Weitbrecht V, Jirka GH. 2001. Flow patterns and exchange processes in dead zones of rivers. *Proceedings of the 2001 International Symposium on Environmental Hydraulics. ISEH and IAHR*. 439–445.

Weitbrecht V, Socolofsky SA, Jirka GH. 2007. Experiments on mass exchange between groin fields and main stream rivers. *Journal of Hydraulic Engineering* **134**: 173–183.

Wood P, Armitage P. 1997. Biological effects of fine sediment in the lotic environment. *Environmental Management* **21**: 203–217.

Yossef M, de Vriend H. 2010. Sediment exchange between a river and its groyne fields: Mobile-bed experiment. *Journal of Hydraulic Engineering* **136**: 610–625.

Zanke U. 1977. *Berechnung der Sinkgeschwindigkeiten von Sedimenten*. Heft 46. Franzius-Instituts für Wasserbau: Hanover.

Supporting information

Additional supporting information may be found online in the supporting information tab for this article.